Fluid–structure interaction simulations to investigate the asymmetrical pattern and energy transfer during vocal fold vibrations ⊘

Guofeng He (iD) ; Qilin Liu ✉ (iD) ; Weibing Cai (iD) ; Azure Wilson (iD) ; Mohammad Hossein Doranehgard;
Lea Sayce (iD) ; Haoxiang Luo (iD) ; Zheng Li ✉ (iD)

Check for updates

View Online Export Citation

Articles You May Be Interested In

Two-scale structure of the current layer controlled by meandering motion during steady-state collisionless driven reconnection

Phys. Plasmas (July 2004)

Fluid–structure interaction simulations to investigate the asymmetrical pattern and energy transfer during vocal fold vibrations

View Online   Export Citation   CrossMark

Guofeng He,[1] (iD) Qilin Liu,[1,a)] (iD) Weibing Cai,[1] (iD) Azure Wilson,[1] (iD) Mohammad Hossein Doranehgard,[1,2]
Lea Sayce,[3] (iD) Haoxiang Luo,[4] (iD) and Zheng Li[1,a)] (iD)

AFFILIATIONS

[1]Department of Mechatronics Engineering, Morgan State University, Baltimore, Maryland 21251, USA
[2]Department of Mechanical Engineering, Johns Hopkins University, Baltimore, Maryland 21218, USA
[3]Department of Communication Science and Disorders, School of Health and Rehabilitation Sciences,
 University of Pittsburgh, Pittsburgh, Pennsylvania 15260, USA
[4]Department of Mechanical Engineering, Vanderbilt University, Nashville, Tennessee 37212, USA

Note: This paper is part of the Special Topic, Flow and Phonation.
[a)]Authors to whom correspondence should be addressed: qilin.liu@morgan.edu and zheng.li@morgan.edu

ABSTRACT

Asymmetrical vocal fold vibration is the cause of many voice problems. In this study, a two-dimensional fluid–structure interaction model is developed with the finite element method in COMSOL Multiphysics. The vocal folds with asymmetric stiffness are simulated and compared with the symmetric vocal folds as well as unilateral immobile vocal folds. The vocal fold vibration pattern and energy exchange between the fluid and vocal fold structure are analyzed. The results show that the unilateral vocal fold paralysis (UVFP) and the stiffness difference between the two vocal folds would lead to a decrease in the vibration amplitude compared with symmetrical conditions. The asymmetrical vocal fold vibration allows a frequency lock-in between two sides of the vocal fold, and the lock-in frequency is sensitive to the vocal fold stiffness. The vocal fold vibration can maintain a quasi-periodic pattern when the stiffness difference is less than 5 MPa. 10 MPa stiffness difference can trigger a transition from the quasi-periodic state to the chaotic state. The energy conversion efficiency between fluid and structure is reduced in the presence of a stiffness difference and under UVFP conditions. This efficiency is further decreased when chaotic vibration happens, indicating the importance of vibration regularity in maintaining effective fluid-to-structure energy transfer.

I. INTRODUCTION

Phonation is a biomechanically intricate process that plays a fundamental role in human vocal communication. Voice production primarily occurs in the larynx, where the vibration of the vocal folds constitutes the principal source of acoustic energy. Each year, approximately 7.6% of adults in the United States (nearly 17.9×10^6 individuals) are reported to experience voice disorders (Bhattacharyya, 2014). The majority of voice disorders are attributed to involuntary muscular activity within the larynx (Van Houtte et al., 2010). A comprehensive understanding of the mechanisms underlying voice production is crucial for the effective prevention and clinical management of such disorders.

The vibration of the vocal folds is induced by the pressurized airflow from the lungs. The interaction between the airflow and the vocal fold tissue, referred to as fluid–structure interaction (FSI), is responsible for generating self-sustained, periodic oscillations that produce the primary acoustic signal. The sound wave is subsequently modulated by the articulatory structures, including the oral cavity, tongue, and lips, to form intelligible speech (Pramanik et al., 2024). In this process, the vocal fold vibration directly influences the pitch, loudness, and timbre of the produced voice. Unilateral vocal fold paralysis (UVFP) is a common voice disorder characterized by the impaired vibratory function of one vocal fold, typically resulting from neural or muscular damage. UVFP impairs the regulation of pitch and loudness, leading to significant difficulties in verbal communication and social interaction (Chhetri et al., 2013; Ishizaka and Isshiki, 1976). By analyzing the frequency and waveform of vocal fold vibration, pathological features of UVFP can be

identified, thereby providing a scientific basis for surgical intervention (Alku *et al.*, 2002).

Both *in vivo* and *ex vivo* experimental methodologies have been employed to investigate the dynamics of vocal fold vibration. *In vivo* experiments enable direct visualization of vocal fold vibration through high-speed endoscopy. However, this technique is limited in its ability to capture airflow characteristics and the underlying FSI dynamics (Kniesburges *et al.*, 2011). In contrast, *ex vivo* experiments facilitate the visualization of the laryngeal airflow field, thereby providing critical insights into FSI mechanisms. The *ex vivo* experiments commonly utilize animal models with laryngeal anatomies comparable to that of humans, such as rabbits (Li *et al.*, 2021b) and non-human primates (Nishimura *et al.*, 2022). These studies have demonstrated the feasibility and efficacy of employing animal laryngeal models to investigate human laryngeal function (Fernandes *et al.*, 2025). Nonetheless, the high cost and complexity associated with animal-based experiments pose significant limitations. As a practical alternative, simplified laryngeal models offer a cost-effective and highly controllable platform for investigating laryngeal biomechanics. Among these, as proposed by Scherer *et al.* (2001a) and later extended and refined through their subsequent studies (Scherer *et al.*, 2001b; 2010), a mechanical model termed M5 has been widely employed for modeling the larynx. The M5 model has been improved to analyze the material properties of the vocal fold, the effect of the false vocal fold (Becker *et al.*, 2009), and the multi-layer structure of the vocal fold (Mendelsohn and Zhang, 2011), etc. In addition to structural investigations, the M5 model has also been utilized to analyze aerodynamic phenomena such as glottal jet flow (Audier *et al.*, 2016) and airborne propagation of respiratory droplets (Fritzsche *et al.*, 2022). In the present study, the M5 model is employed to analyze the FSI characteristics associated with asymmetric vocal fold vibrations.

In addition to experimental approaches, numerical simulation is another important method for investigating asymmetric vocal fold motion. Li *et al.* (2021b) employed asymmetric Young's modulus value for the bilateral vocal folds to investigate the vocal fold vibration in both healthy and simulated UVFP conditions. Their findings revealed a 10%–11% difference in frequency between the two sides. Xue *et al.* (2014) simulated tension imbalance by reducing the Young's modulus of one vocal fold by 20%, successfully reproducing phase-shifted and amplitude-asymmetrical vibration patterns. Naseri and Razavi (2023) modeled UVFP by assigning significantly higher stiffness to one side of the vocal fold, effectively reproducing the asymmetrical vibratory dynamics observed before and after medialization laryngoplasty (a common surgical intervention). These studies demonstrate that the vibration patterns characteristic of UVFP primarily arise from stiffness asymmetry between the vocal folds. To model the vocal fold dynamics, some studies have employed the mass-spring model, in which the vocal folds are simplified using either two-mass or collective-mass representations. Xue *et al.* (2010) developed a two-mass model and reported a nonlinear vibration behavior under conditions of tension imbalance. As the imbalance became severe, the glottal flow transitioned from a periodic regime to quasi-periodic variations. They also demonstrated that tension imbalance has a pronounced nonlinear effect on the fundamental frequency of vocal fold vibration. However, these mass-spring models typically assume the vocal fold only deforms in the lateral direction. In contrast, continuum models are capable of simulating hyperelasticity behavior and dynamic deformations that

more closely approximate physiological conditions (Chen *et al.*, 2020; Li *et al.*, 2020; and McCollum *et al.*, 2023). These models can be further refined to incorporate anatomical features such as the vocal fold cover and the false vocal folds (Xue *et al.*, 2014; Zheng *et al.*, 2009). The fidelity of these models can be enhanced through the integration of anatomical data obtained from advanced medical imaging techniques, such as magnetic resonance imaging (MRI) and computed tomography (CT) (Li *et al.*, 2021b; McCollum *et al.*, 2023; Mittal *et al.*, 2011; and Xue *et al.*, 2010). Continuum models offer valuable insights into the stress distribution and deformation patterns within the vocal folds. Therefore, in the present study, a continuum model is employed to investigate the effect of stiffness asymmetry on vocal fold vibration.

Phonation involves a continuous energy exchange between the vocal folds and the glottal airflow, which drives and sustains vocal fold oscillation. Titze (1980) reported that during the opening phase of vocal fold vibration, the kinetic energy of airflow is transferred to the vocal fold. In this process, the vocal fold is pushed and accelerated by the aerodynamic pressure on the vocal fold surface. During the closing phase, the vocal fold transfers kinetic energy back to the airflow. Part of the kinetic energy is dissipated during the process due to factors such as the boundary layer effect (Titze, 1980), damping within the tissue, and tissue contact at the vocal fold medial surface (Motie-Shirazi *et al.*, 2021; Zhang *et al.*, 2006). This bidirectional energy exchange supports the self-sustained oscillation of the vocal folds, which is essential for human voice production (Motie-Shirazi *et al.*, 2021). It also plays a critical role in vocal efficiency and may have implications for the onset and progression of voice disorders (Ringenberg *et al.*, 2021). The dynamics of energy transfer during symmetric vocal fold vibration have been investigated in several studies. Sundström *et al.* (2025) and Titze (1980) analyzed energy exchange in the steady-state oscillatory regime, reporting both the distribution of kinetic energy in the airflow and the mechanical work performed by surface pressure on the vocal fold tissue. However, the mechanisms of energy exchange during asymmetric vocal fold vibration remain not well understood and warrant further investigation. Therefore, the objective of the present study is to investigate the energy exchange associated with asymmetric vocal fold vibration.

In light of these, the present work aims to investigate the inherently nonlinear dynamic effects of stiffness difference, thereby shedding light on mechanisms of energy exchange during asymmetric vocal fold vibration. A continuum-based two-dimensional (2D) FSI model is developed in COMSOL Multiphysics using a finite element method to investigate the effects of stiffness asymmetry on vocal fold vibration. This model simulates the condition of UVFP and asymmetrical vibration by introducing asymmetry in the material properties of the vocal folds. The vibratory patterns and energy conversion between the airflow and vocal folds are analyzed to understand the phonation of abnormal vocal folds, which are meaningful for the diagnosis of voice disorders.

II. PHYSICAL MODEL AND FSI MODEL DEVELOPMENT

The vocal fold vibration is simulated with a two-dimensional model as shown in Fig. 1. The vocal folds are placed in the rectangular larynx model at 20 mm from the entrance, with width $W = 20$ mm, height $D = 20$ mm, and medial thickness $T = 1.75$ mm. The initial gap between the two vocal folds is 0.4 mm. These dimensions of the vocal folds are based on the M5 model, which was often employed for vocal
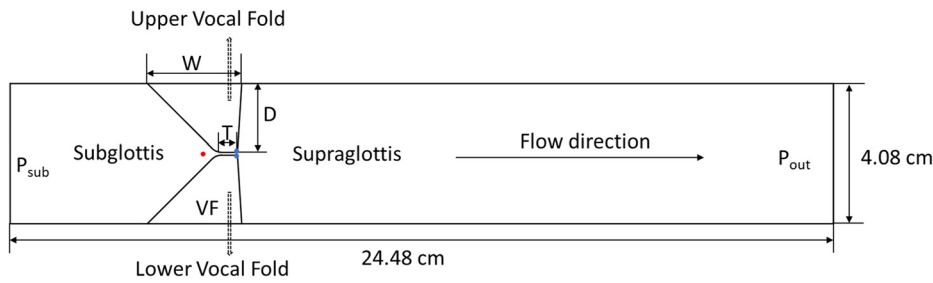
FIG. 1. The computational domain of the 2D vocal fold model. The red and blue dots are the monitoring locations for the pressure and displacement, respectively.

fold vibration simulations (Chen *et al.*, 2020; Li *et al.*, 2020; 2021a; and Tian *et al.*, 2014).

In the rectangular channel shown in Fig. 1, the airflow is characterized by density $\rho_f = 1.13\,\text{kg/m}^3$ and kinematic viscosity $\nu_f = 0.000\,23\,\text{Pa s}$. A typical subglottal driving pressure at 1 kPa is applied, which results in an estimated intraglottal jet velocity of $V = \sqrt{2(\Delta P)/\rho_f} \approx 42\,\text{m/s}$. We define the characteristic Reynolds number $Re_j = Vd/\nu_f = 210$, where $d = 1\,\text{mm}$ is the characteristic glottal gap during the opening phase (Chen *et al.*, 2020; Li *et al.*, 2020; 2021a; and Tian *et al.*, 2014). Therefore, the flow is assumed to be laminar (details in Subsection 2 of the Appendix), viscous, and incompressible. The flow is governed by the Navier–Stokes equation, which is written as follows:

$$\begin{cases} \dfrac{\partial u}{\partial x} + \dfrac{\partial v}{\partial y} = 0, \\[2mm] \dfrac{\partial u}{\partial t} + u\dfrac{\partial u}{\partial x} + v\dfrac{\partial u}{\partial y} = -\dfrac{1}{\rho_f}\dfrac{\partial p}{\partial x} + \nu_f\left(\dfrac{\partial^2 u}{\partial x^2} + \dfrac{\partial^2 u}{\partial y^2}\right), \\[2mm] \dfrac{\partial v}{\partial t} + u\dfrac{\partial v}{\partial x} + v\dfrac{\partial v}{\partial y} = -\dfrac{1}{\rho_f}\dfrac{\partial p}{\partial y} + \nu_f\left(\dfrac{\partial^2 v}{\partial x^2} + \dfrac{\partial^2 v}{\partial y^2}\right), \end{cases} \quad (1)$$

where u, v, and p are the Cartesian velocity components and the pressure, respectively.

The vocal folds are assumed to be homogeneous material. Their deformations are modeled by the two-parameter Saint Venant–Kirchhoff model, which is a hyperelastic model. This model is one of the commonly employed models to represent large deformations of soft tissues in vocal fold research (Chen *et al.*, 2020; Li *et al.*, 2020; 2021a; 2021b; and Wex *et al.*, 2015). The strain energy density function in this model is given as (Muhr, 2005)

$$W = \frac{\lambda}{2}(tr(\mathbf{E}))^2 + \mu \cdot tr(\mathbf{E}^2), \quad (2)$$

where $\mathbf{E}$ is the Green–Lagrange strain tensor, defined as $\mathbf{E} = \frac{1}{2}(\mathbf{F}^T\mathbf{F} - \mathbf{I})$, $\mathbf{I}$ is the identity matrix, $\mathbf{F}$ is the deformation gradient tensor. λ and μ are the Lamé parameters, defined as follows:

$$\lambda = \frac{E\nu}{(1+\nu)(1-2\nu)}, \quad (3)$$

$$\mu = \frac{E}{2(1+\nu)}, \quad (4)$$

where E is Young's modulus and $\nu = 0.475$ is Poisson's ratio. To investigate the effect of stiffness on vocal fold vibration, two groups of vocal

folds with baseline stiffness values, $E = 30$, and 60 kPa, respectively, are modeled in this study. These values are selected based on previous literature and are within the physiologically reasonable range for vocal fold tissue (Alipour and Vigmostad, 2012; Cook *et al.*, 2008; and Li *et al.*, 2021a; 2021b). The cases with the same Young's modulus on both sides of the vocal fold represent healthy conditions. To simulate UVFP, the upper vocal fold is fixed at a closed position. The asymmetrical vibration is modeled by reducing the stiffness of the upper vocal fold. The stiffness values of the vocal folds are listed in Table I for all the cases; the density of vocal fold tissue is $\rho_s = 1040\,\text{kg/m}^3$.

Rayleigh damping is employed to simulate the energy dissipation characteristics of the tissue. The Rayleigh damping vector ($\mathbf{C}$) is written as follows (Hall, 2006):

$$\mathbf{C} = \alpha\mathbf{M} + \beta\mathbf{K}, \quad (5)$$

where $\mathbf{M}$ is the mass matrix and $\mathbf{K}$ is the stiffness matrix. α and β, respectively, are coefficients of the mass and stiffness, which are calculated as follows:

$$\alpha = 4\pi f_1 f_2 \frac{\zeta f_2 - \zeta f_1}{f_2^2 - f_1^2}, \quad (6)$$

$$\beta = \frac{\zeta f_2 - \zeta f_1}{\pi(f_2^2 - f_1^2)}, \quad (7)$$

where $\zeta = 0.01$ is the damping ratio. f_1 and f_2, respectively, are the first and second eigenfrequencies of the vocal folds.

The airflow passes the rectangular larynx model from the subglottic side to the supraglottic side. The inflow is assumed to be fully developed, driven by inlet pressure $P_{sub} = 1\,\text{kPa}$. The outlet pressure is set to the reference pressure at $P_{out} = 0\,\text{Pa}$. The walls of the rectangular

TABLE I. Vocal fold stiffness.

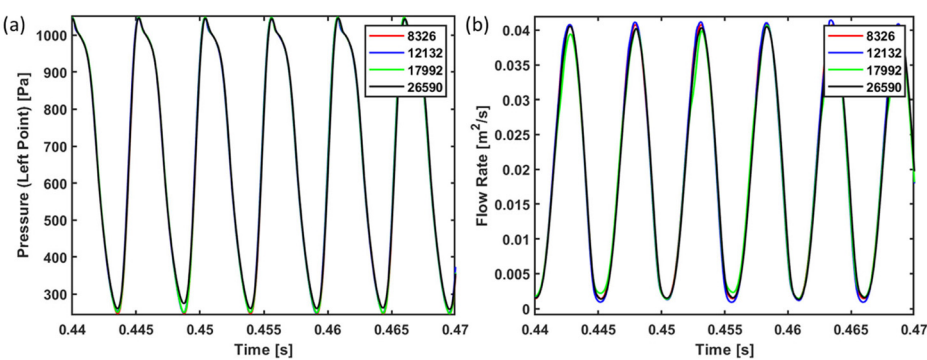|	Young's modulus (kPa)	
Case ID	Upper vocal fold	Lower vocal fold
S1C1	30	30
S1C2	Fixed	30
S1C3	25	30
S1C4	20	30
S2C1	60	60
S2C2	Fixed	60
S2C3	55	60
S2C4	50	60

FIG. 2. The grid-independent study for (a) comparison of pressure at a point (red point marked in Fig. 1) and (b) flow rate.

channel and the vocal fold surfaces are no-slip and no-penetration boundaries for the flow field. The base of the vocal fold is the fixed boundary at which the motion of the vocal fold is constrained. To handle vocal fold contact and maintain flow domain continuity, a minimum glottal gap of 0.1 mm was enforced during the simulation (Li et al., 2021a).

The present FSI model is developed in commercial software COMSOL Multiphysics. The airflow is modeled with the Laminar Flow module. Both the velocity and pressure fields are discretized by second-order elements, together with a consistent stabilization scheme. The vocal fold tissue, represented as a hyperelastic medium, is modeled with the Solid Mechanics module. The displacement field is discretized by cubic elements. The interaction between the airflow and the vocal fold is captured via the FSI interface using deformable mesh. The solution of flow and solid fields is solved by a fully coupled algorithm. The time integration is performed implicitly by employing the generalized-α method. The time step is $\Delta t = 3 \times 10^{-5}$ s for both the fluid and the solid solvers, as determined from a time step independence study. At each time step the solution is solved by the Newton iteration method with a convergence criterion 1×10^{-6}. Each simulation is conducted until a well-defined dynamic equilibrium is achieved as characterized by a fully developed airflow. A validation of the FSI model is provided in Subsection 1 of the Appendix.

For case S1C1 (healthy case, both sides have 30 kPa stiffness), simulation results on grids with 8326–26 590 elements are compared in Fig. 2. Pressure at the subglottic side (red point in Fig. 1) and the flow rate are shown in Figs. 2(a) and 2(b), respectively. The results from these simulations collapse on each other, showing a grid convergency of flow field simulation. For simulations of the vocal fold motion, frequency and amplitude of vocal fold vibration are compared in Table II. The amplitude is measured by the y-displacement of the point at the glottal exit. In Table II, the frequency is the same for these simulations. Seen from the amplitude, the grid with more than 12 132 elements does not significantly improve the results, so the grid with 12 132 elements is sufficient for the present study. It should be noted

that the grid 12 132 has a maximum element size of 0.7 cm. Assuming at least 12 elements per wavelength of sound (Marburg, 2008), this maximum element size corresponds to a cutoff frequency of about 4000 Hz, which is high enough for the present investigation.

III. RESULTS AND DISCUSSION

A systematic investigation of the cases listed in Table I is presented in this section to elucidate how stiffness asymmetry affects phonation. The analysis examines the vibration pattern of the vocal fold and the associated energy transfer during the FSI process. The vibration patterns are examined through (1) the flow field and stress distribution in the vocal folds and (2) nonlinear vibratory behaviors characterized by frequency, amplitude, and dynamic phase space patterns. As mentioned in the Introduction, the present study, in addition to the energy analyses of symmetrical vocal fold vibration, examines the energy conversion in asymmetrical vibration.

A. Flow field and stress in vocal folds

The flow field and deformation data of the vocal fold are available from the simulation for all eight cases (see Subsection 2 of the Appendix). Here, we focus on cases S1C1 and S1C2, which represent the healthy and UVFP conditions, respectively. Figure 3 shows the lateral displacement of the vocal fold tip for case S1C1. The lateral displacement is measured at the blue dot on the lower vocal fold as marked in Fig. 1. The flow is sampled after time t_0, after which the airflow becomes fully developed. A complete oscillation cycle of the lower vocal fold is marked in blue in Fig. 3, on which nine instances are selected for analysis, as marked by T0–T8 in sequence.

The flow in the vocal fold channel and the stress on the vocal folds are shown in Figs. 4 and 5, respectively. In Fig. 4, the vortical flow of cases S1C1 and S1C2 are compared for a regular cycle of vocal fold motion. In both cases, a train of vortical structures concentrates near the vocal fold and then weakens gradually streamwise. The vortical structures are initially a pair of vortex sheets with opposite signs at the exit of the vocal fold. These vortex sheets quickly roll up to form a pair of eddies that are rotating in opposite directions. In case S1C1, as shown in Fig. 4(a), the scale of eddies in count-clock-wise-rotating and clock-wise-rotating are similar. In case S1C2, as shown in Fig. 4(b), the flow field seems dominated by a clock-wise-rotating eddy, which is entraining with the surrounding count-clock-wise-rotating eddies. These results suggest that the asymmetry of vocal fold motion affects the development of vortical structures, at least in the region near the vocal fold.

TABLE II. Frequency and amplitude of vocal fold vibration.

Element number	8326	12 132	17 992	26 590
Frequency (Hz)	192	192	192	192
Amplitude (mm)	0.70	0.73	0.71	0.72
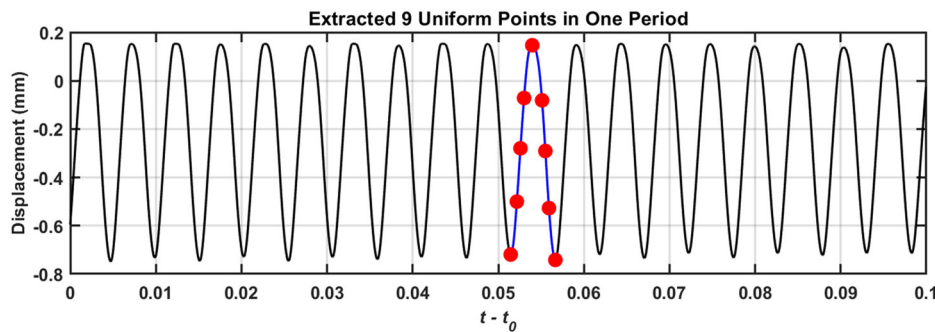
The distribution of von Mises stress in the vocal folds is compared in Fig. 5 for cases S1C1 and S1C2. During the vocal fold closure phase, as shown in Fig. 5(a), from T0 to T4, the stress concentrates at two side surfaces of the vocal fold at T0, then the stress propagates into the vocal fold and concentrates at the base of the vocal fold at T4. During the opening phase, as shown in Fig. 5(b) from T4 to T8, the stress propagates inversely from the base to the two side surfaces of the vocal fold to finish a cycle of the stress changing. In Fig. 5(b), the stress variation is relatively mild in the mobile vocal fold, showing the effect of asymmetric motion in the solid deformation.

In summary, the results of cases S1C1 and S1C2 have revealed significant differences when there is an asymmetry in the material properties on two sides of the vocal fold. Similar results are observed in other cases (see Subsection 2 of the Appendix).

B. Nonlinear analysis of vocal fold vibrations

1. Asymmetry vibration parameters

The frequency and amplitude of vocal fold vibration are compared in Table III for the cases listed in Table I. The vibration is measured by the lateral displacement of the monitor points as marked by blue dots in Fig. 1. In Table III, the fundamental frequency is the dominant frequency estimated by the fast Fourier transform of the displacement signal. The amplitude is the maximum absolute of the displacement averaged in the range of $t - t_0 = 0$–0.1 s.

For healthy conditions, as in cases S1C1 and S2C1 listed in Table III, the results for two sides of the vocal fold match with each other, which is essential for effective phonation. In comparison with case S1C1, case S2C1 exhibits a lower amplitude and higher fundamental frequency, which is consistent with the increased stiffness in S2C1. The fundamental frequencies of cases S1C1 and S2C1 are 190 and 250 Hz, respectively. Similar results are observed in Li et al. (2021a), where a vocal fold with a stiffness of 30 kPa exhibits a fundamental frequency of about 190 Hz, and the 60 kPa one approximates to 260 Hz. These results show the reliability of the present simulations. For the UVFP condition, both cases S1C2 and S2C2 exhibit a significant reduction in vibration amplitude, while the fundamental frequency of the deformable side is close to that in the healthy condition. When the upper side of the vocal fold is softer than the lower one, as in cases S1C3 and S2C3 in Table III, the two sides of the vocal fold are locked at the same fundamental frequency, whose value is slightly lower than that of the healthy condition. The softer side exhibits a lower amplitude than that of the stiffer side, and for both sides, the amplitude is lower than that in the healthy condition.

In comparison with S1C3 and S1C4, the lock-in frequency disappears, and the amplitude of both sides increases. In comparison with S2C3 and S2C4, although the amplitude in these two cases is similar, the vibration in S2C4 is found to transition into a chaotic pattern, so no fundamental frequency is identified. From these results, whether there is a lock-in frequency or not depends on the stiffness difference as well as the stiffness itself. These results are also reported by Xue et al. (2014), who reported similar reductions in frequency and amplitude under conditions of superior–inferior tension imbalance.

2. Dynamical analysis of vibration

To visualize the state of the dynamic system, the waveform of displacement together with the recurrence plot and three-dimensional (3D) phase of the state vector are plotted in Figs. 6–13 for the cases in Table I. The state vector $x_i = [x(t_i), x(t_i + \tau), x(t_i + 2\tau)]$ is equipped with time series of displacement $x(t)$ with a time delay τ. The $\tau = 1.5 \times 10^{-3}$ s is determined using the first minimum of the Mutual Information (MI) function (Fraser and Swinney, 1986; Doranehgard et al., 2024). The recurrence plot is a contour of the recurrence matrix, which is defined as

$$R_{i,j} = \Theta\left(\epsilon - \left\|x_i - x_j\right\|\right), \qquad (8)$$

where Θ is the Heaviside function, defined as $\Theta = 1$ for $x \geq 0$ and $\Theta = 0$ for $x < 0$. The recurrence threshold ϵ is set to 0.25 in this study to make the recurrence plot clear. $\|\cdot\|$ denotes the Euclidean norm. The recurrence plot marks an instance when the system revisits similar states in phase space. In the recurrence plot, the diagonal lines, isolated points, and disrupted structures, respectively, indicate the temporal regularity and the potential emergence of nonlinear and chaotic behavior of the system states (Doranehgard et al., 2024). The 3D phase plot visualizes the state vector x_i in coordinates of $[t, t + \tau, t + 2\tau]$. In the 3D phase plot, the trajectory in the shape of a ring is typically associated with quasi-periodic behavior, while the dispersed or fragmented shapes indicate the chaotic vibrations (Liu et al., 2024). Figure 6 presents the results of case S1C1, which is the healthy condition with Young's modulus at 30 kPa. In Figs. 6(a) and 6(b), it can be seen that the waveforms of the displacement in the upper and lower vocal folds are similar, suggesting a synchronized motion between the two sides. In Figs. 6(b) and 6(e), the recurrence plots of the upper and lower vocal folds both display clear, evenly spaced diagonal lines with noticeable width. This result indicates a quasi-periodic pattern. Correspondingly,
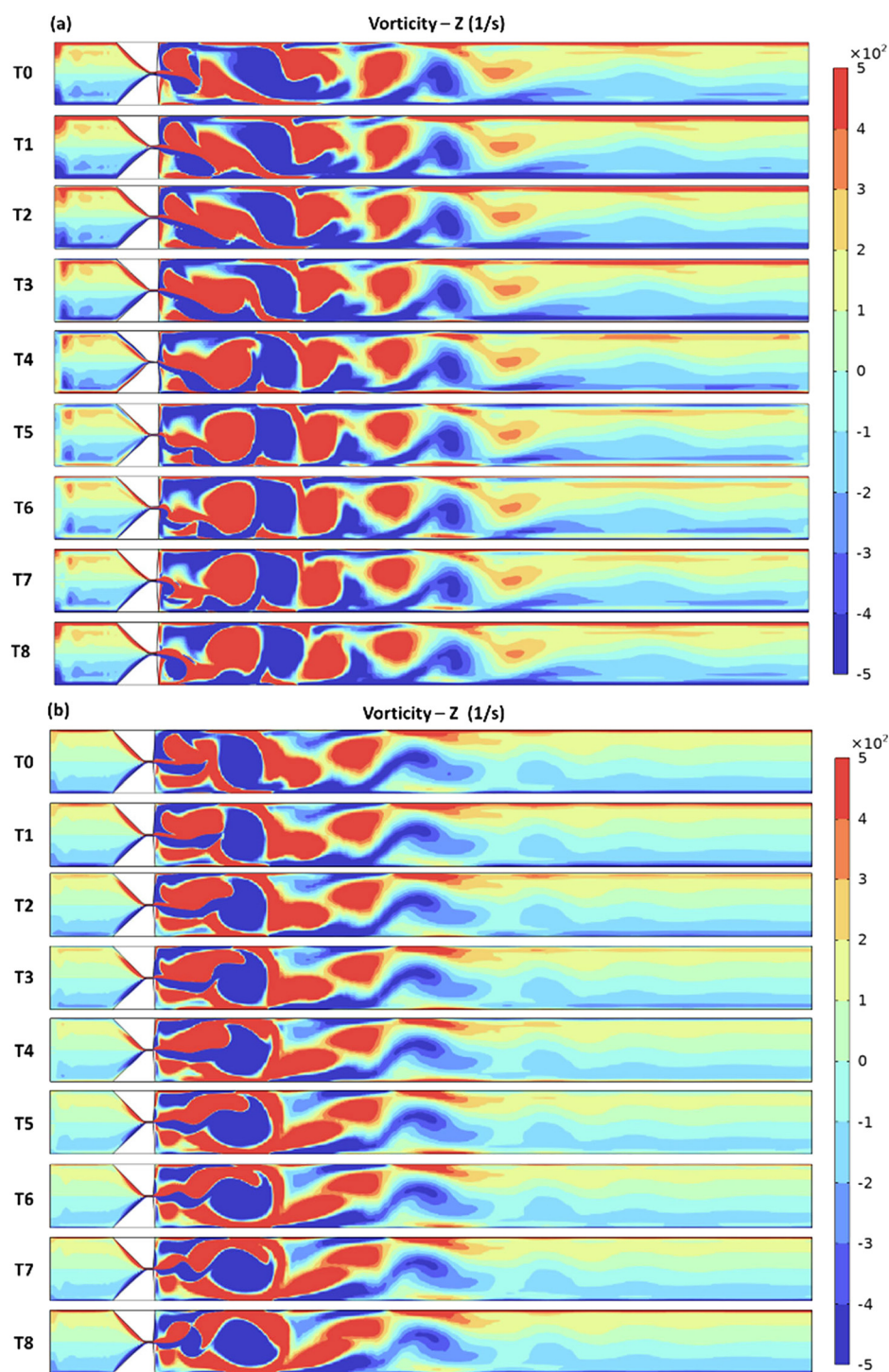
FIG. 4. The vorticity field during a regular cycle of vocal fold motion. Cases (a) S1C1 and (b) S1C2 represent the healthy and UVFP conditions, respectively.

the three-dimensional phase portraits, in Figs. 6(c) and 6(f), exhibit closed-loop, ring-shaped trajectories for both folds, which further confirm the presence of a quasi-periodic pattern. These results suggest that in symmetric (healthy) conditions, vocal fold vibration follows a quasi-periodic pattern. A similar quasi-periodic pattern is also found in Xue *et al.* (2010).

Figure 7 shows the results of case S1C2, which is the case of UVFP with Young's modulus at 30 kPa on the lower vocal fold. In
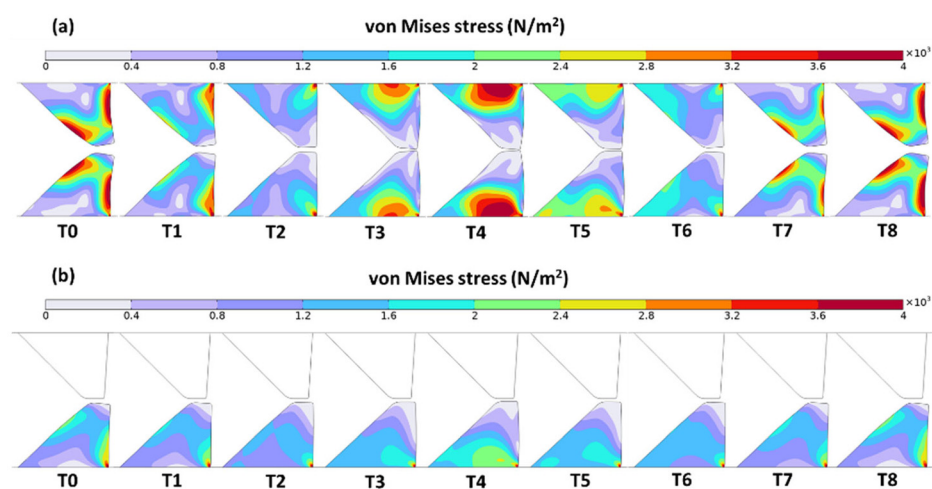
FIG. 5. The distribution of von Mises stress during a regular cycle of vocal fold motion. Cases (a) S1C1 and (b) S1C2 represent the healthy and UVFP conditions, respectively.

TABLE III. The characteristic parameters of asymmetry vocal fold vibration.

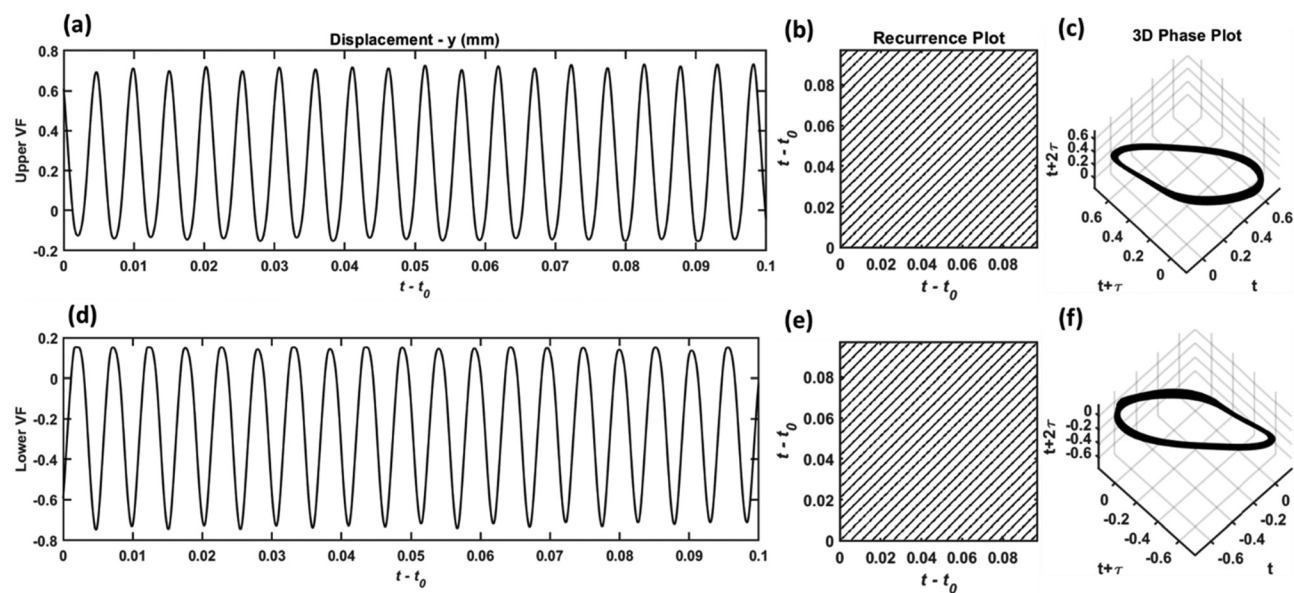| Case ID	Fundamental frequency (Hz)		Average amplitude (mm)	
	Upper vocal fold	Lower vocal fold	Upper vocal fold	Lower vocal fold
S1C1	190	190	0.72	0.73
S1C2	Fixed	180	Fixed	0.46
S1C3	190	190	0.36	0.46
S1C4	160	190	0.52	0.72
S2C1	250	250	0.37	0.37
S2C2	Fixed	250	Fixed	0.13
S2C3	250	250	0.15	0.17
S2C4	⋯	⋯	0.14	0.12

FIG. 6. Dynamic behavior of vocal fold vibration in case S1C1 for (a) and (d) displacement, (b) and (e) recurrence plots, and (c) and (f) 3D phase space plots. (a)–(c) are results of the upper vocal fold. (d)–(f) are results of lower vocal folds.
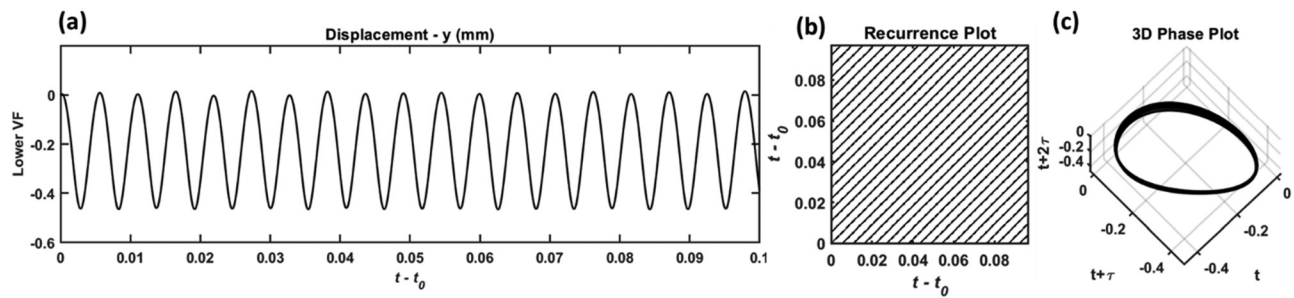
FIG. 7. Dynamic behavior of vocal fold vibration in case S1C2 for (a) displacement, (b) recurrence plot, and (c) 3D phase space plot.
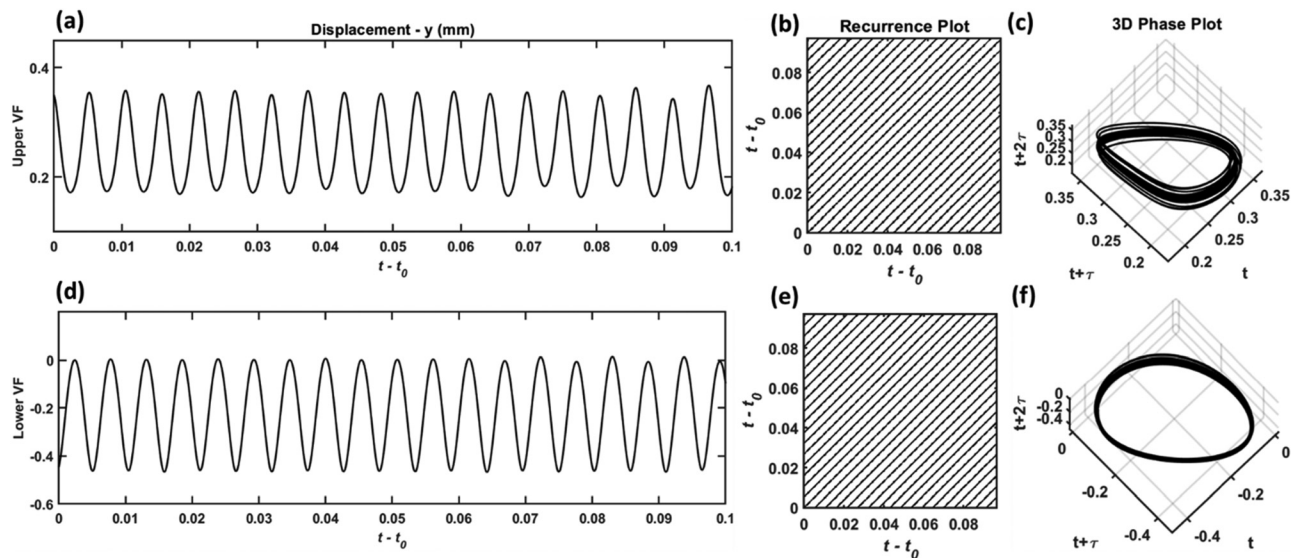

FIG. 8. Dynamic behavior of vocal fold vibration in case S1C3 for (a) and (d) displacement, (b) and (e) recurrence plots, and (c) and (f) 3D phase space plots. (a)–(c) are results of the upper vocal fold. (d)–(f) are results of lower vocal folds.

Fig. 7, the upper vocal fold in case S1C2 is fixed and therefore not considered in the nonlinear dynamic analysis. In Fig. 7(a), the lower vocal fold exhibits a vibration pattern that is regular over time. In Fig. 7(b), the recurrence plot of case S1C2 presents clear and parallel diagonal structures, which indicate a quasi-periodic state similar to that observed in Figs. 6(b) and 6(e). This behavior is further supported by the 3D phase trajectory shown in Fig. 7(c), which forms a smooth, closed loop. Therefore, the system presents a quasi-periodic pattern when one side of the vocal fold is fixed.

Figure 8 shows the results of case S1C3, in which the Young's modulus for upper and lower vocal folds are 25 and 30 kPa, respectively. In Figs. 8(a) and 8(b), the waveform of the displacement is stable, showing a regular motion. In Figs. 8(b) and 8(e), the recurrence plots of case S1C3 present clear and parallel diagonal lines on both sides of the vocal fold. This feature is similar to that observed in the healthy case (S1C1), which indicates a quasi-periodic pattern. The 3D phase portraits are shown in Figs. 8(c) and 8(f) for the upper and lower sides of the vocal fold, respectively. In these 3D phase portraits, although the trajectories are in the shape of a toroidal, they are less

coincidental than that observed in Fig. 6(c) for case S1C1. Thus, although the vibration pattern is quasi-periodic, the effects of stiffness difference can be captured by the 3D phase portraits, in which the deviation from a periodic trajectory emerges.

Figure 9 shows the results of the case S1C4, in which the Young's modulus for the upper and lower vocal folds are 20 and 30 kPa, respectively. Results of the lower vocal fold are shown in Figs. 9(d)–9(f). A quasi-periodic pattern is observed for the case S1C4, which is similar to that in cases S1C1–S1C3. Results of the upper vocal fold are shown in Figs. 9(a)–9(c). In Fig. 9(a), the displacement of the upper vocal fold demonstrates an amplitude modulation. In Fig. 9(b), although localized concretions of points are observed, the recurrence plot still exhibits a pattern of parallel diagonal lines. The corresponding phase portrait shown in Fig. 9(c) maintains a toroidal-like structure, with trajectories distributed around a central region in the phase space. These features suggest that the vibration remains quasi-periodic in nature. Compared to Fig. 9(f), the more dispersed trajectory in the phase portrait indicates that early signs of nonlinear dynamics have begun to emerge. Thus, the
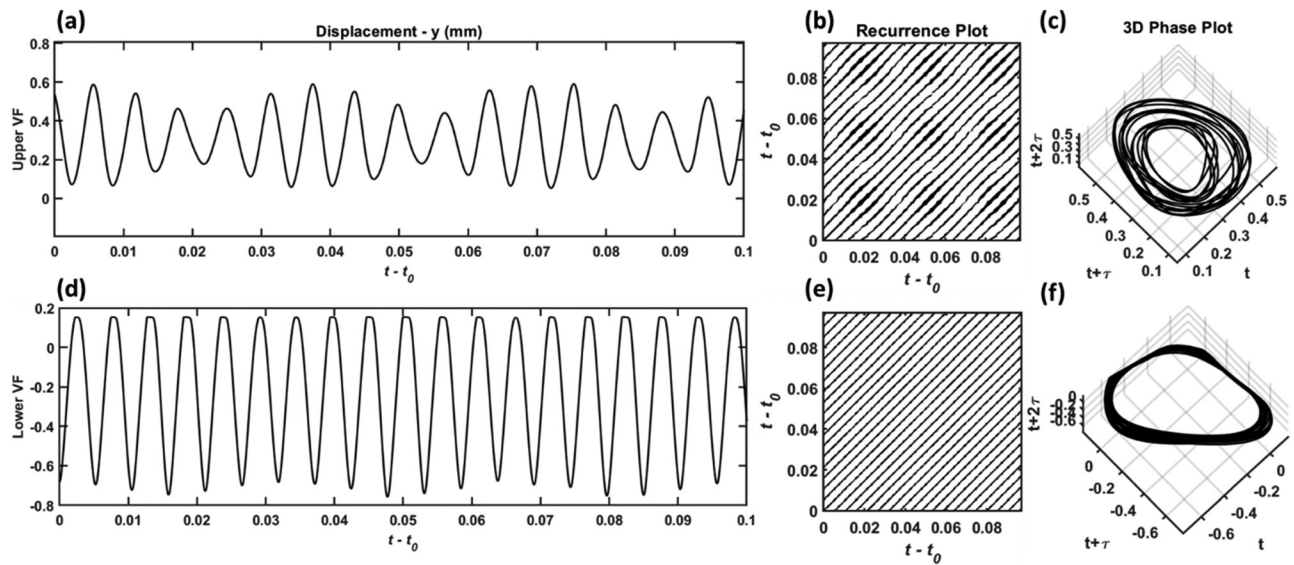
FIG. 9. Dynamic behavior of vocal fold vibration in case S1C4 for (a) and (d) displacement, (b) and (e) recurrence plots, and (c) and (f) 3D phase space plots. (a)–(c) are results of the upper vocal fold. (d)–(f) are results of lower vocal folds.

FIG. 10. Dynamic behavior of vocal fold vibration in case S2C1 for (a) and (d) displacement, (b) and (e) recurrence plots, and (c) and (f) 3D phase space plots. (a)–(c) are results of the upper vocal fold. (d)–(f) are results of lower vocal folds.
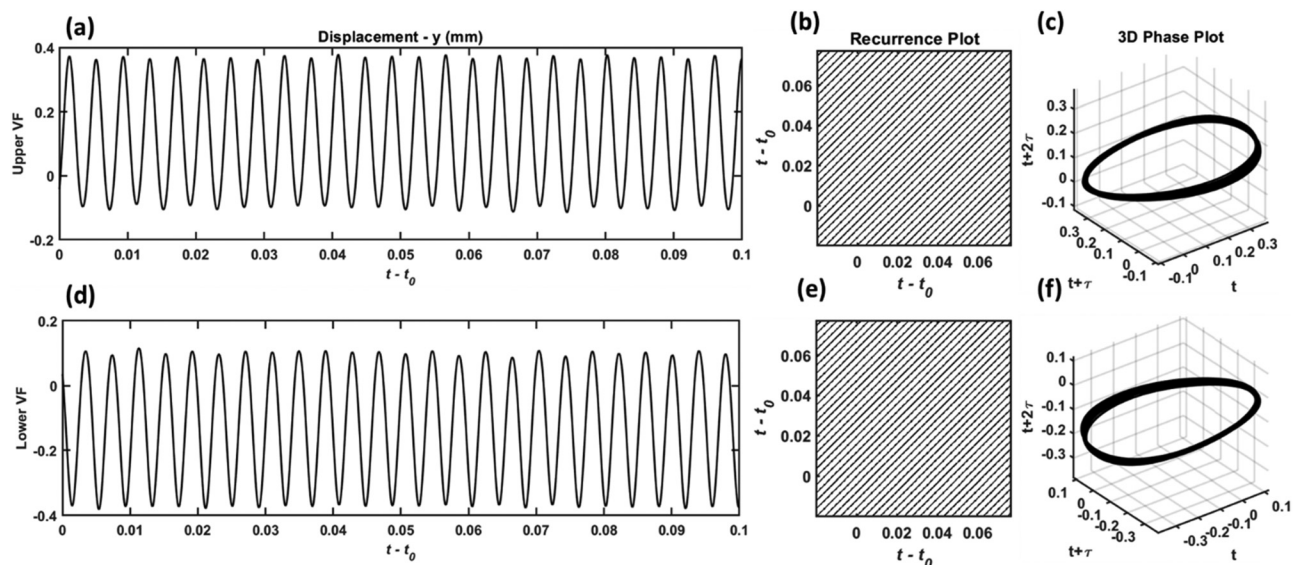
stiffness difference triggers a transition from the quasi-periodic state to the chaotic state.

Figure 10 shows the results of case S2C1, which is the healthy condition with Young's modulus at 60 kPa. In the first and second rows of Fig. 10, the results of the upper and lower vocal folds show similarity, suggesting a synchronized motion between the two sides. In Figs. 10(a) and 10(d), it can be seen that both the upper and lower vocal folds exhibited regular oscillatory behavior and the displacements of the two sides of the vocal fold are symmetrical. In Figs. 10(b)

and 10(e), the recurrence plots of S2C1 revealed a series of evenly spaced, narrow diagonal lines. The corresponding 3D phase portrait, in Figs. 10(c) and 10(f), displays a thin, well-defined toroidal structure centered in phase space. Therefore, similar to case S1C1, the vocal fold vibration under healthy conditions appears as a quasi-periodic pattern.

Figure 11 shows the results of case S2C2, which is the UVFP with Young's modulus of the lower vocal fold at 60 kPa. In Fig. 11(a), the lower vocal fold is found exhibiting a regular motion. In Fig. 11(b), the recurrence plot clearly shows an evenly spaced diagonal structure. In
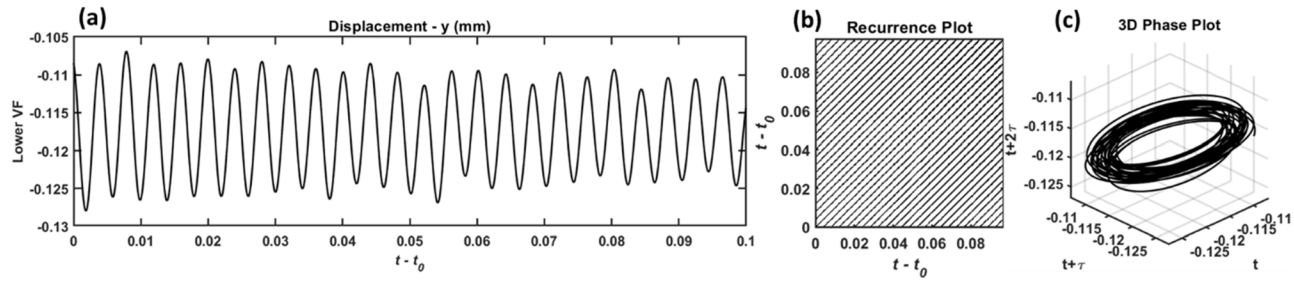
17 September 2025 16:03:22

FIG. 11. Dynamic behavior of vocal fold vibration in case S2C2 for (a) displacement, (b) recurrence plot, and (c) 3D phase space plot.

FIG. 12. Dynamic behavior of vocal fold vibration in case S2C3 for (a) and (d) displacement, (b) and (e) recurrence plots, and (c) and (f) 3D phase space plots. (a)–(c) are results of the upper vocal fold. (d)–(f) are results of lower vocal folds.
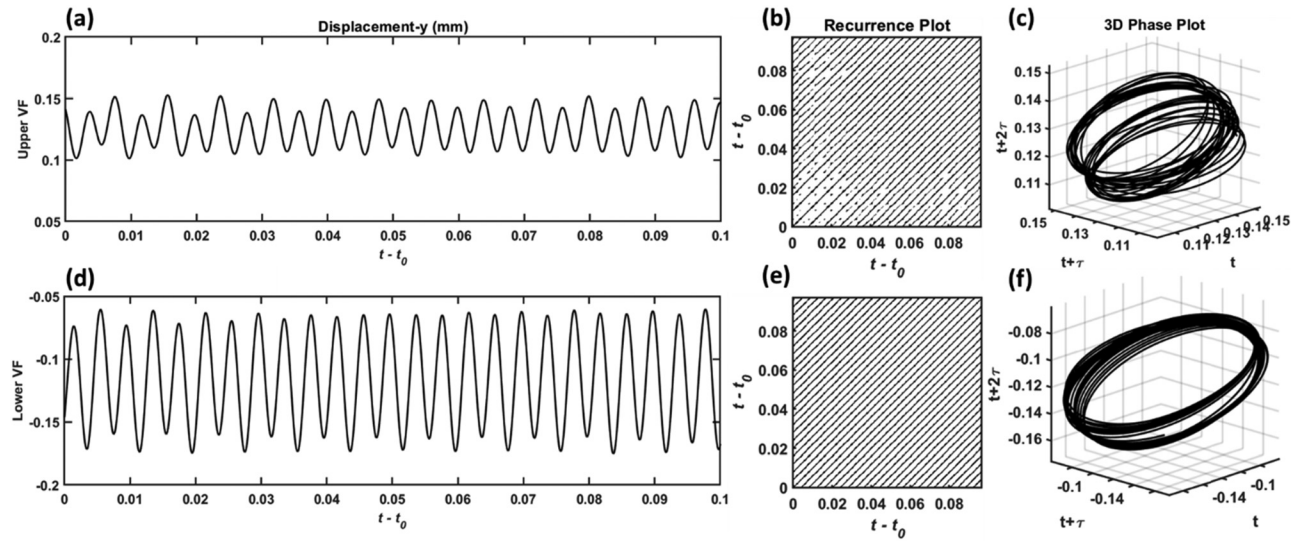

FIG. 13. Dynamic behavior of vocal fold vibration in case S2C4 for (a) and (d) displacement, (b) and (e) recurrence plots, and (c) and (f) 3D phase space plots. (a)–(c) are results of the upper vocal fold. (d)–(f) are results of lower vocal folds.
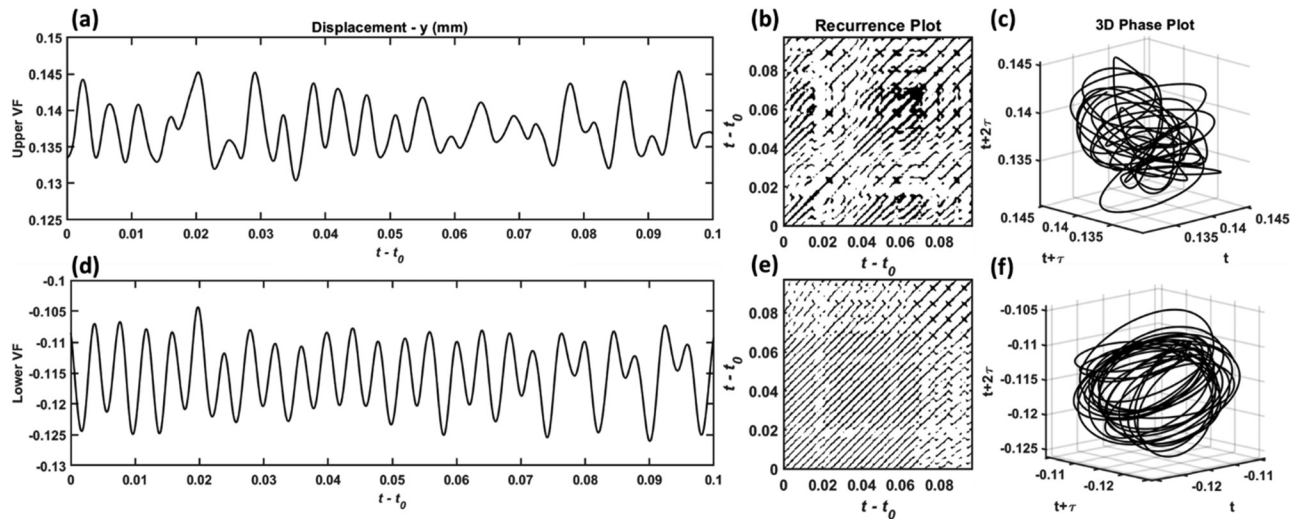
Fig. 11(c), although the phase portrait is more dispersive than that of the healthy condition in Fig. 10(f), the closed toroidal trajectory remains bounded and continuous, suggesting the vibration pattern in case S2C2 is quasi-periodic. The stiffness of case S2C2 is higher than that of case S1C2. Therefore, the system is able to maintain a quasi-periodic pattern when one side of the vocal fold is fixed, although the stiffness of the vocal fold is increased.

Figure 12 shows the results of case S2C3, in which the Young's moduli of the upper and lower vocal folds are 55 and 60 kPa, respectively. In Fig. 12(a), the displacement of the upper vocal fold exhibits amplitude variation, which indicates the onset of chaos, although the dominant oscillatory behavior remained quasi-periodic. In Fig. 12(b), the recurrence plot of the upper vocal fold displays evenly spaced parallel diagonal lines, which is characteristic of quasi-periodicity. It may be observed that the dots in Fig. 12(b) are not uniform, which suggests the occurrence of nonlinearity. In Fig. 12(c), the 3D phase portrait is bounded and continuous, further confirming the quasi-periodic nature of the dynamics. However, the trajectory in Fig. 12(c) is less concentrated than that of the case S2C1 in Fig. 10(c), indicating a transitional state toward chaos. The results of the lower vocal fold, as shown in Figs. 12(d)–12(f), are similar to those observed in Figs. 10 and 11, which suggest that the lower vocal fold maintains a quasi-periodic vibration pattern. However, in Fig. 12(f), the phase trajectory appears more dispersed than that in Fig. 10(f). Considering that the stiffness of the lower vocal fold is the same between cases S2C3 and S2C1, the dispersed trajectory in the lower vocal fold is probably caused by the coupling between the upper and lower vocal folds.

Figure 13 presents the results of case S2C4, in which the upper and lower vocal folds have asymmetric Young's moduli of 50 and 60 kPa, respectively. Under this condition, the vibratory behavior of the vocal fold deviates from regular periodic motion. As shown in Fig. 13(a), the displacement of the upper fold shows that the amplitude is fluctuating, and the waveform is distorted. These results indicate a strong nonlinear dynamic of the upper fold. The recurrence plot shown in Fig. 13(b) exhibits fragmented and scattered patterns, which suggest a breakdown of quasi-periodic dynamics. This result is supported in Fig. 13(c), as the trajectory becomes chaotic, where the trajectory becomes highly disordered and no longer forms a toroidal structure. In Fig. 13(d), the lower vocal fold also deviates from regular motion, which is evidenced by irregular oscillation and amplitude modulation. In Fig. 13(e), although some parallel lines remained, the recurrence plot showed partially broken diagonal lines with dispersion. The 3D phase portrait in Fig. 13(f) reveals a disordered trajectory, which is much more tangled than that in Fig. 9(c). Considering that the stiffness of the lower vocal fold is the same between cases S2C4 and S2C1, the disordered trajectory in the lower vocal fold suggests an underlying interconnection between the two sides of the vocal folds, by which both the upper and lower vocal folds have entered a chaotic regime. Such a chaotic pattern differs from the quasi-periodic one reported by Xue et al. (2010).

C. Energy transfer

The energy transfer during the FSI process is quantified by the averaged kinetic energy variation of the flow and the averaged work done by the flow to the vocal fold. From a control volume point of view, the pressure input at the inlet is converted to the kinetic energy of the flow and the energy of the vocal folds. Once vibration is established, the energy of the vocal folds is constant, and the pressure input at the inlet is mostly supplied to the kinetic energy of the flow except for the damping in the system. Thus, the ratio between the vocal fold kinetic energy and the flow kinetic energy could be viewed as a criterion for efficiency. Results of the case S1C1 are provided in Fig. 14 as an example. The averaged kinetic energy of the flow is calculated by integration as follows:
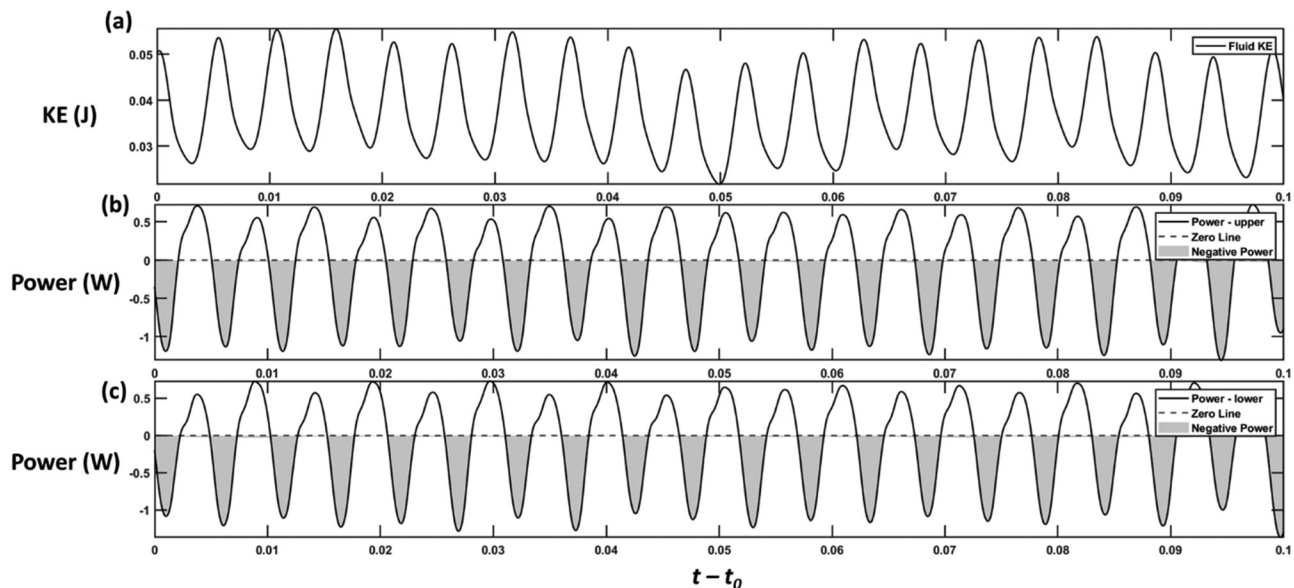
FIG. 14. The kinetic energy of flow (a) and power of the vocal folds (b) and (c) along time for S1C1. (b) and (c) The power for the upper and lower VF, respectively; the negative power is marked in gray.

$$\overline{KE} = \frac{1}{t_1 - t_0} \int_{t_0}^{t_1} \int_S \frac{1}{2} \rho_f (u^2 + v^2) dS dt, \quad (9)$$

where S is the computational domain of the flow field in Fig. 1. t_0 and t_1 are shown in Figs. 6(a)–13(a), with $t_1 - t_0 = 0.1$. The power of work done by fluid on the vocal fold is calculated for each side of the vocal fold via

$$P(t) = \int_L p v_n dx, \quad (10)$$

where L is the surface of the vocal fold. p is the pressure on the surface. v_n is the normal component of the fluid velocity on L, which points from the fluid side to the solid side. The negative power means the pressure is driving the motion of the vocal fold, and thus, the energy is transferred from the flow into the vocal fold. As marked in gray in Figs. 14(b) and 14(c), the negative part of the power is then integrated over time to obtain the work done by the fluid pressure on the vocal fold surface, as follows:

$$W_{neg,i} = \int_{t_i}^{t_{i+1}} P_{neg}(t) dt, \quad (11)$$

where power $P_{neg}(t)$ is less than zero during the time range $[t_i, t_{i+1}]$. To quantify the work for both the quasi-periodic and the chaotic state of the motion, the averaged work is calculated over the time of energy variation, as follows:

$$\overline{W}_{neg} = \frac{1}{N} \sum_i^N W_{neg,i}, \quad (12)$$

where N is the number of cycles.

The ratio $B = \overline{W}_{neg}/\overline{KE}$ quantifies the energy contribution from the fluid to the vibration of the vocal fold, and it is used here to represent the conversion efficiency of the kinetic energy. B_u and B_l are the ratio of the upper and lower vocal folds, respectively. $B_t = B_u + B_l$ represents a conversion efficiency of the vocal folds. The ratios of the cases in Table I are listed in Table IV. For healthy conditions, as in cases S1C1 and S2C1 in Table IV, the B_u and B_l are close to each other. For UVFP conditions, as in cases S1C2 and S2C2 in Table IV, the lower vocal fold exhibits a reduced percentage compared to the healthy

TABLE IV. The average kinetic energy and the proportion of work done by the fluid pressure on VF.

| Case ID | Ratio between work and kinetic energy, B | | | |
	Upper vocal fold, B_u (%)	Lower vocal fold, B_l (%)	$B_t = B_u + B_l$ (%)	$\overline{KE}$ (J)
S1C1	4.42	4.45	8.86	0.0377
S1C2	0	3.86	3.86	0.0168
S1C3	2.39	2.11	4.50	0.0342
S1C4	2.19	3.40	5.59	0.0418
S2C1	2.88	2.94	5.82	0.0261
S2C2	0	0.174	0.174	0.0117
S2C3	0.496	0.665	1.16	0.0226
S2C4	0.213	0.228	0.441	0.0251

condition. In the case groups S1C1–S1C4, case S1C2 yields the lowest $\overline{KE}$ in the fluid domain. The case S2C2 also yields the lowest $\overline{KE}$ in case groups S2C1–S2C4. These results confirm the severe impact of UVFP on vibratory dynamics and energy exchange. For cases with asymmetric stiffness, like cases S1C3, S1C4, S2C3, and S2C4, the ratio B_t is less than 65% of that of the healthy one but is still higher than that in the UVFP condition. These results suggest that the stiffness difference tends to decline the conversion efficiency of the kinetic energy. For the case with Young's modulus 30 kPa in lower vocal fold, as in cases S1C3 and S1C4, B_l tends to increase as the stiffness difference grows. This trend is consistent with the amplitude analysis, where greater oscillation is observed for the lower vocal fold in Table III. For the case with Young's modulus 60 kPa in the lower vocal fold, as in cases S2C3 and S2C4 in Table IV, B_l is found decrease as the asymmetry grows. Considering the quasi-periodic vibration in Fig. 12 and the chaotic one in Fig. 13, this result is probably due to the conversion efficiency of the kinetic energy being low when the vibration of vocal folds is chaotic.

In summary, the energy conversion efficiency declines when two sides of the vocal fold have stiffness differences, especially in cases of UVFP. For two sides of the vocal fold, the energy transfers are similar in cases of symmetric stiffness. The asymmetrical stiffness alters the work done on each side of the vocal fold and reduces the energy conversion efficiency. Notably, chaotic vibrations, as seen in case S2C4, further decrease the conversion efficiency, highlighting the critical role of vibration regularity in maintaining effective fluid-to-structure energy transfer.

IV. CONCLUSION

The influence of stiffness difference, in the range of 0–10 MPa, on vocal fold vibration pattern and energy transfer is investigated, for vocal folds with stiffness in the range of 30–60 MPa. The vocal fold vibration amplitude, frequency, and displacement pattern are analyzed. The kinetic energy of airflow and the pressure work on the vocal fold surface are calculated to quantify the energy conversion between the airflow and the vocal folds. The main conclusions are summarized as follows:

(1) The UVFP and the stiffness difference are responsible for the decrease in amplitude. When the stiffness difference is less than 5 MPa, the vocal fold vibration allows a frequency lock-in between the two sides, and the lock-in frequency depends on the stiffness of the stiffer side.

(2) The vibration pattern is quasi-periodic for the cases in symmetric and UVFP conditions. When the stiffness difference is less than 5 MPa, the vibration is still capable of maintaining a quasi-periodic pattern. As the stiffness difference reaches 10 MPa, the vibration exhibits a transition from the quasi-periodic state to the chaotic state, and this transition becomes more pronounced for the stiffer vocal fold.

(3) The energy conversion efficiency is balanced between two sides of the vocal fold when stiffness is symmetric. This efficiency declines in the presence of a stiffness difference and under UVFP conditions. The stiffness difference alters the work done to each side of the vocal fold and can induce chaotic vibration. The energy conversion efficiency is further decreased when chaotic vibration happens, indicating the importance of vibration

regularity in maintaining effective fluid-to-structure energy transfer.

These findings may have implications for therapeutic interventions and clinical diagnostics. In particular, the observed link between stiffness difference and vibration stability suggests that keeping the stiffness difference within an appropriate range could help maintain stable vibration patterns and effective energy transfer, which are important for voice quality. This may provide a biomechanical reference for guiding treatment adjustments, such as tuning implant tension or injection material stiffness, and for evaluating recovery after clinical intervention.

V. CURRENT SHORTCOMINGS

In this study, the vocal folds are modeled in a two-dimensional domain, which cannot fully capture the complex coupling behavior present in three-dimensional structures. Establishing a three-dimensional model will help improve the accuracy and applicability of the study. Based on our current understanding, three-dimensional effects could modify the quantitative predictions. From the fluid-flow side, spanwise instabilities could strengthen the unstable vibrations seen in 2D, giving similar or stronger instability. From the fluid–structure coupling side, the extra constraints from the two fixed surfaces on each vocal fold might reduce the motion, leading to weaker instability.

The nonlinear viscoelastic properties of biological tissues and the mechanical differences between tissue layers are not fully considered in the present model, which may affect the accuracy of energy conversion results. In the future, experimental measurements will be combined to obtain more accurate material parameters of tissue so as to improve the physiological relevance of the model. Our group is also working on three-dimensional fluid–structure interaction simulations to study the nonlinear vibration behavior of asymmetrical vocal folds, and the results will be reported in future publications.

AUTHOR DECLARATIONS
Conflict of Interest

The authors have no conflicts to disclose.

Author Contributions

Guofeng He: Conceptualization (equal); Data curation (equal); Formal analysis (equal); Investigation (equal); Methodology (equal); Software (equal); Validation (equal); Visualization (equal); Writing – original draft (equal); Writing – review & editing (equal). **Qilin Liu:** Conceptualization (equal); Data curation (equal); Formal analysis (equal); Investigation (equal); Methodology (equal); Software (equal); Writing – review & editing (equal). **Weibing Cai:** Conceptualization (equal); Methodology (equal); Software (equal). **Azure Wilson:** Conceptualization (equal); Methodology (equal). **Mohammad Hossein Doranehgard:** Conceptualization (equal); Methodology (equal); Writing – review & editing (equal). **Lea Sayce:** Conceptualization (equal); Formal analysis (equal); Investigation (equal); Supervision (equal); Writing – review & editing (equal). **Haoxiang Luo:** Conceptualization (equal); Data curation (equal); Formal analysis (equal); Investigation (equal); Methodology (equal); Supervision (equal); Validation (equal); Visualization (equal); Writing – review & editing (equal). **Zheng Li:** Conceptualization (equal); Data curation (equal); Formal analysis (equal); Funding acquisition (equal); Investigation (equal); Methodology (equal); Project administration (equal); Resources (equal); Software (equal); Supervision (equal); Validation (equal); Visualization (equal); Writing – review & editing (equal).

DATA AVAILABILITY

The data that support the findings of this study are available from the corresponding authors upon reasonable request.

APPENDIX: SUPPLEMENTARY REMARKS ON MODELING

1. Validation of the FSI model

To validate the computational model, the motion of a flexible flapper downstream of a cylinder is simulated, and results are compared with available simulation data in the literature. The computational domain is a rectangular channel as shown in Fig. 15. The cylinder, flapper, and up-and-downsides of the channel are no-slip walls. The Reynolds number is based on the averaged inlet velocity $\overline{U}_0$ and the cylinder radius R, is $Re = 2\overline{U}_0 R/\nu_f = 100$. The density ratio between solid structure and fluid flow is 10.
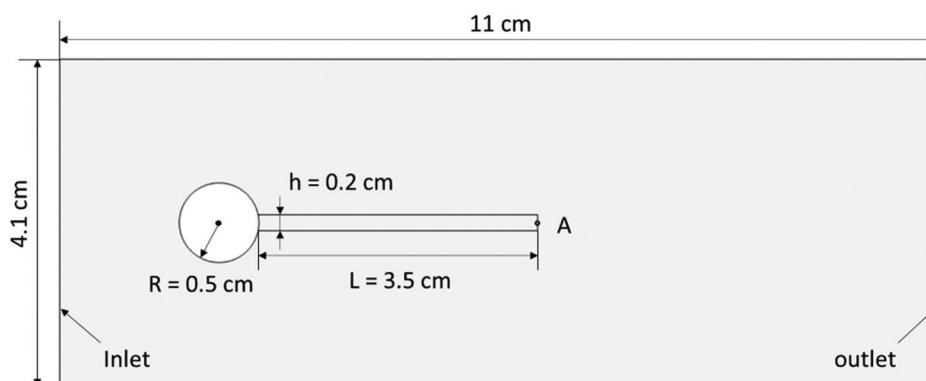
FIG. 15. Computational domain of the flapper downstream of a cylinder. The free end of the flapper is marked by point A.
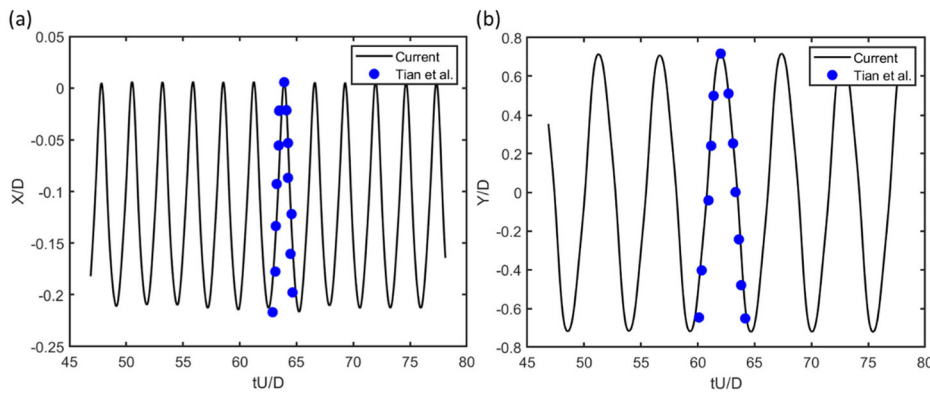
FIG. 16. Displacement at the end of the flapper: (a) x-displacement and (b) y-displacement. The displacement is measured at point A, as marked in Fig. 15.

TABLE V. Amplitude of the y-displacement of the free end, the Strouhal number St, and the drag coefficient.

	$A_m/2R$	St	C_D
Tian *et al.* (2014)	0.78	0.190	4.11
Turek and Hron (2006)	0.83	0.190	4.13
Li *et al.* (2018)	0.81	0.183	4.05
Present results	0.72	0.188	4.42

The displacement of the flapper is shown in Fig. 16. The x- and y-displacements of the point A, as marked in Fig. 15, are shown in Figs. 16(a) and 16(b), respectively. In Fig. 16, both the x- and y-displacements of point A show regular amplitude and are in good agreement with the result from Tian *et al.* (2014). The oscillation magnitude A_m, the Strouhal number of the y-displacement, and the average drag coefficient C_D are listed in Table V, and are compared with results from Tian *et al.* (2014), Turek and Hron (2006), and Li *et al.* (2018). The Strouhal number is defined as $St = 2fR/\overline{U}_0$ where $f = 2.94$ Hz is the frequency of signal in Fig. 16(b). The average

drag coefficient C_D is defined by $\overline{F}_x/(0.25\rho_f \overline{U}_0^2 R)$, where $\overline{F}_x = 6.38e - 4$ N/m is the average drag of the cylinder-beam system. In Table V, good agreement between present results and the results in the literature shows the validity of the present model.

2. Flow field and deformation data of the vocal fold

Before analyzing the flow field and vocal fold deformation, the velocity distribution at the moment of peak glottal opening, when the maximum velocity occurs, is analyzed to verify the validity of the laminar flow assumption. As shown in Fig. 17(a), the streamwise velocity in the computational domain is visualized by contour lines. The corresponding velocity profiles at five streamwise positions (X_1–X_5) are presented in Figs. 17(b)–17(f). These profiles indicate that the glottal jet is fully developed downstream of the vocal folds, with a peak velocity reaching approximately 50 m/s. Thus, the $Re_j = Vd/\nu_f \approx 217$ is well below the commonly accepted threshold for transition to turbulence in internal flows, which typically transitions to turbulence at $Re > 2000$ (Titze and Martin, 1998). Following this verification, the flow field and solid deformation of the vocal folds were analyzed in detail for cases S1C3, S1C4, and S2C1–S2C4, as presented in Figs. 18 and 19.
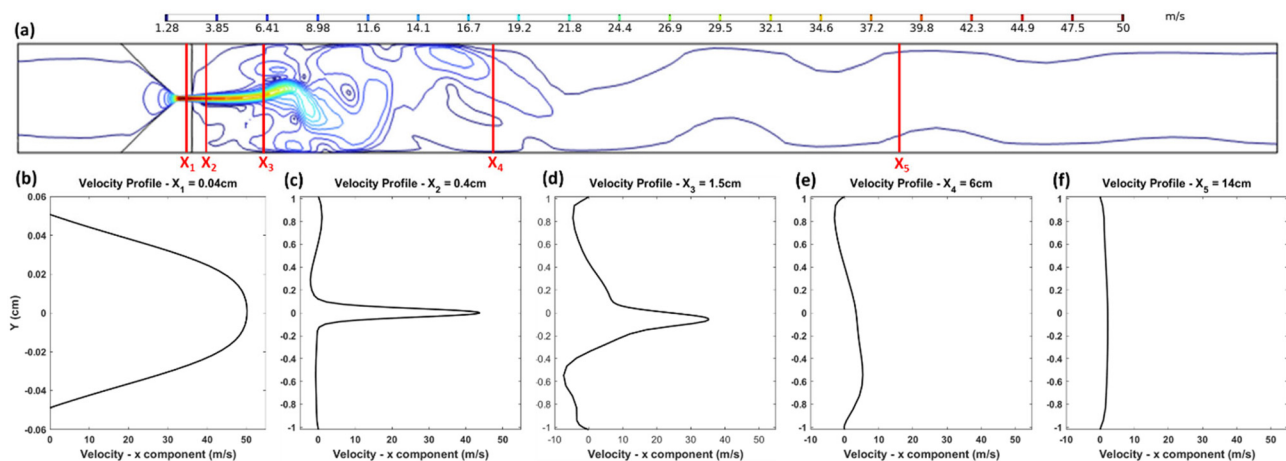

FIG. 17. Velocity field at the moment of peak glottal opening. (a) Contour line of velocity, and (b) velocity profiles at streamwise locations X_1–X_5 = 0.04, 0.4, 1.5, 6, and 14 cm, downstream of the glottis.
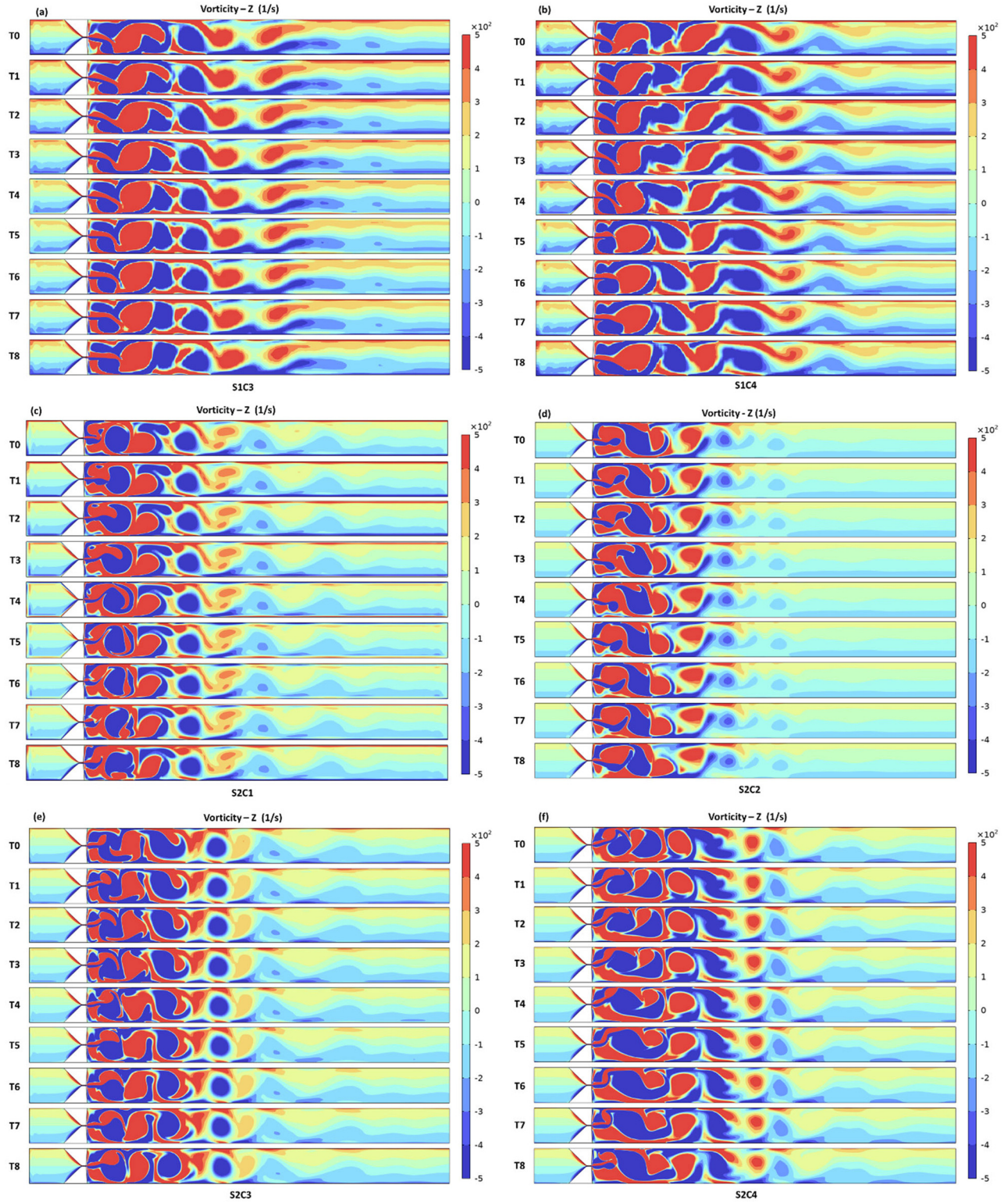
FIG. 18. Spanwise vorticity contour for cases: (a) S1C3, (b) S1C4, (c) S2C1, (d) S2C2, (e) S2C3, and (f) S2C4.
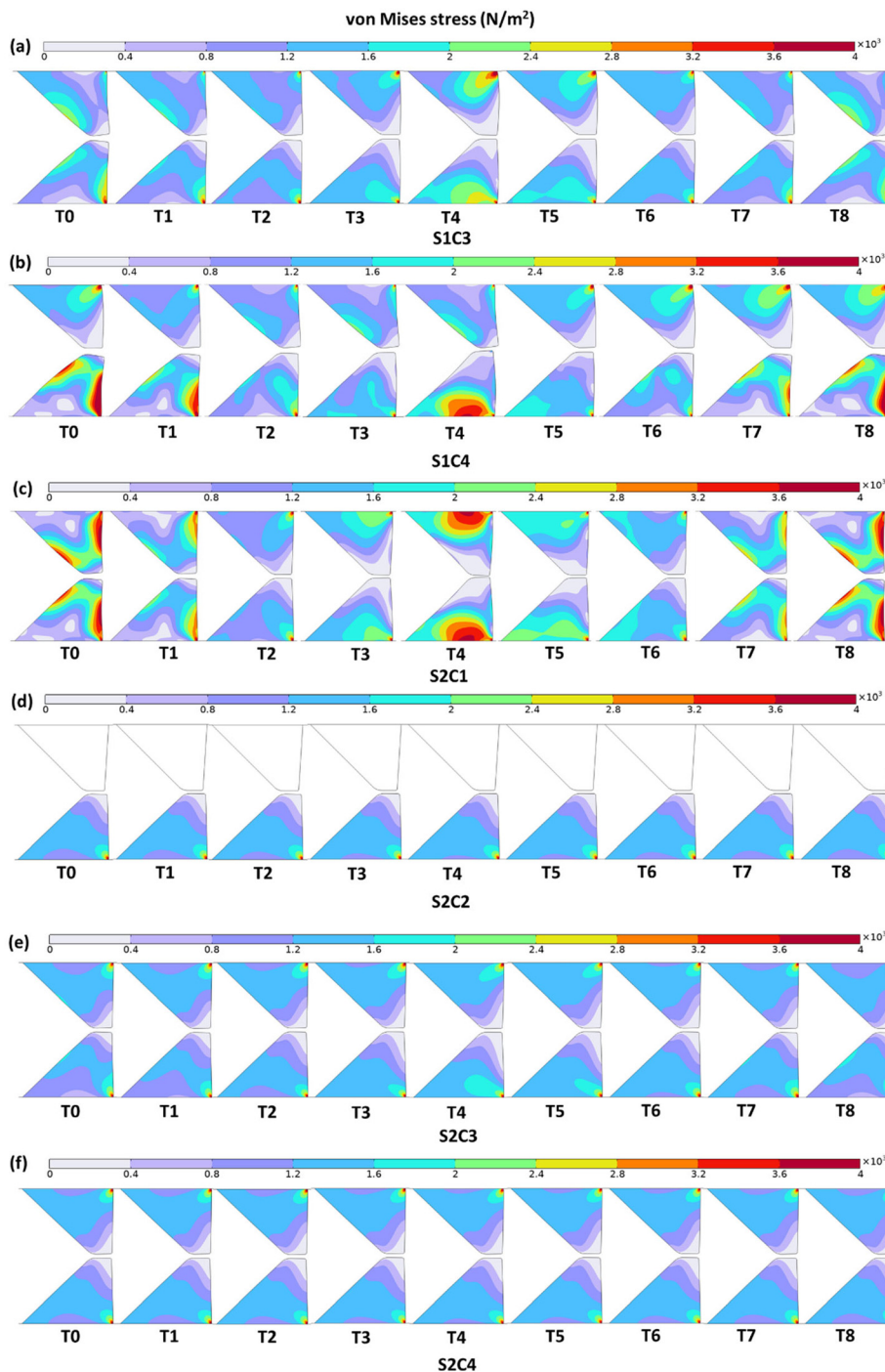
17 September 2025 16:03:22

FIG. 19. von Mises stress distributions of cases: (a) S1C3, (b) S1C4, (c) S2C1, (d) S2C2, (e) S2C3, and (f) S2C4.

For cases S1C3, S1C4, and S2C1–S2S4 in Table I, the results of vortical flow and solid deformation are shown in Figs. 18 and 19, respectively. Figure 18 shows the spanwise component of vorticity by contours. All the cases show similar vortical features. At the vocal fold exit, the vortical structure is a pair of vortex sheets with opposite signs. It rapidly rolls up to form a pair of rotating eddies. These eddies dissipate downstream, and the flow gradually becomes uniform. However, the scale of the vortical structures is different for these cases, as shown in the region near the vocal fold in Fig. 18. Figure 19 shows the von Mises stress by contours. In Fig. 19, each row shows the development of stress during a period of vocal fold motion from time T0 to T8, after the flow is fully developed. From

T0 to T4, the vocal fold is closing. Meanwhile, the distribution of von Mises stress initially concentrates at the two side surfaces of the vocal fold at T0, then propagates inward and accumulates near the vocal fold base at T4. From T4 to T8, the vocal fold is opening. In the meanwhile, the stress propagates inversely from the base toward the two side surfaces, completing a full stress cycle. It is also found that the stress distribution is different between the two sides of the vocal fold for the cases with asymmetric stiffnesses, as shown in Figs. 19(a), 19(b), 19(d), and 19(e). Therefore, similar to those observed in Figs. 4 and 5 for cases S1C1 and S1C2, both the vortical flow and deformation of the vocal folds are affected by the stiffness asymmetry.

REFERENCES

Alipour, F. and Vigmostad, S., "Measurement of vocal folds elastic properties for continuum modeling," J. Voice **26**(6), 816.e21–816.e29 (2012).

Alku, P., Bäckström, T., and Vilkman, E., "Normalized amplitude quotient for parametrization of the glottal flow," J. Acoust. Soc. Am. **112**(2), 701–710 (2002).

Audier, P., Sciamarella, D., and Artana, G., "Pre-switching bifurcation of a slender jet," Phys. Fluids **28**(1), 017103 (2016).

Becker, S., Kniesburges, S., Müller, S., Delgado, A., Link, G., Kaltenbacher, M., and Döllinger, M., "Flow-structure-acoustic interaction in a human voice model," J. Acoust. Soc. Am. **125**(3), 1351–1361 (2009).

Bhattacharyya, N., "The prevalence of voice problems among adults in the United States," Laryngoscope **124**(10), 2359–2362 (2014).

Chen, Y., Li, Z., Chang, S., Rousseau, B., and Luo, H., "A reduced-order flow model for vocal fold vibration: From idealized to subject-specific models," J. Fluids Struct. **94**, 102940 (2020).

Chhetri, B. B. K., Johnsen, F. H., Konoshima, M., and Yoshimoto, A., "Community forestry in the hills of Nepal: Determinants of user participation in forest management," For. Policy Econ. **30**, 6–13 (2013).

Cook, D. D., Nauman, E., and Mongeau, L., "Reducing the number of vocal fold mechanical tissue properties: Evaluation of the incompressibility and planar displacement assumptions," J. Acoust. Soc. Am. **124**(6), 3888–3896 (2008).

Doranehgard, M. H., Karimi, N., Borazjani, I., and Li, L. K. B., "Breaking the symmetry of a wavy channel alters the route to chaotic flow," Phys. Rev. E **109**(4), 045103 (2024).

Fernandes, A. C. N., Ferreira, M. V. N., Serra, L. S. M., Kuckelhaus, S. A. S., Da Silva, E. M., and Sampaio, A. L. L., "Methodological approaches for vocal fold experiments in laryngology: A scoping review," J. Voice **39**, 317 (2025).

Fraser, A. M. and Swinney, H. L., "Independent coordinates for strange attractors from mutual information," Phys. Rev. A **33**(2), 1134–1140 (1986).

Fritzsche, L., Schwarze, R., Junghans, F., and Bauer, K., "Toward unraveling the mechanisms of aerosol generation during phonation," Phys. Fluids **34**(12), 121904 (2022).

Hall, J. F., "Problems encountered from the use (or misuse) of Rayleigh damping," Earthquake Eng. Struct. Dyn. **35**(5), 525–545 (2006).

Ishizaka, K. and Isshiki, N., "Computer simulation of pathological vocal-cord vibration," J. Acoust. Soc. Am. **60**(5), 1193–1198 (1976).

Kniesburges, S., Thomson, S. L., Barney, A., Triep, M., Šidlof, P., Horáček, J., Brücker, C., and Becker, S., "In vitro experimental investigation of voice production," Curr. Bioinf. **6**(3), 305–322 (2011).

Li, Z., Chen, Y., Chang, S., and Luo, H., "A reduced-order flow model for fluid–structure interaction simulation of vocal fold vibration," J. Biomech. Eng. **142**(2), 021005 (2020).

Li, Z., Chen, Y., Chang, S., Rousseau, B., and Luo, H., "A one-dimensional flow model enhanced by machine learning for simulation of vocal fold vibration," J. Acoust. Soc. Am. **149**(3), 1712–1723 (2021a).

Li, Z., Wilson, A., Sayce, L., Avhad, A., Rousseau, B., and Luo, H., "Numerical and experimental investigations on vocal fold approximation in healthy and simulated unilateral vocal fold paralysis," Appl. Sci. **11**(4), Article 4 (2021b).

Li, Z., Xu, X., Li, K., Chen, Y., Huang, G., Chen, C., and Chen, C.-H., "A flapping vortex generator for heat transfer enhancement in a rectangular airside fin," Int. J. Heat Mass Transfer **118**, 1340–1356 (2018).

Liu, G., Yang, M., and Ying, X., "Effects of inlet boundary conditions on nonlinear characteristics in numerical risers," Phys. Fluids **36**(6), 063326 (2024).

Marburg, S., "Discretization requirements: How many elements per wavelength are necessary," in *Computational Acoustics of Noise Propagation in Fluids—Finite and Boundary Element Methods*, edited by S. Marburg and B. Nolte (Springer Berlin Heidelberg, 2008), pp. 309–332.

McCollum, I., Badr, D., Throop, A., and Zakerzadeh, R., "Biotransport in human phonation: Porous vocal fold tissue and fluid–structure interaction," Phys. Fluids **35**(12), 121909 (2023).

Mendelsohn, A. H. and Zhang, Z., "Phonation threshold pressure and onset frequency in a two-layer physical model of the vocal folds," J. Acoust. Soc. Am. **130**(5), 2961–2968 (2011).

Mittal, R., Zheng, X., Bhardwaj, R., Seo, J. H., Xue, Q., and Bielamowicz, S., "Toward a simulation-based tool for the treatment of vocal fold paralysis," Front. Physiol. **2**, 19 (2011).

Motie-Shirazi, M., Zañartu, M., Peterson, S. D., and Erath, B. D., "Vocal fold dynamics in a synthetic self-oscillating model: Intraglottal aerodynamic pressure and energy," J. Acoust. Soc. Am. **150**(2), 1332–1345 (2021).

Muhr, A. H., "Modeling the stress-strain behavior of rubber," Rubber Chem. Technol. **78**(3), 391–425 (2005).

Naseri, M. and Razavi, S. E., "Towards modeling of phonation and its recovery in unilateral vocal fold paralysis by fluid-structure interaction," Bioimpacts **13**(6), 488–494 (2023).

Nishimura, T., Tokuda, I. T., Miyachi, S., Dunn, J. C., Herbst, C. T., Ishimura, K., Kaneko, A., Kinoshita, Y., Koda, H., Saers, J. P. P., Imai, H., Matsuda, T., Larsen, O. N., Jürgens, U., Hirabayashi, H., Kojima, S., and Fitch, W. T., "Evolutionary loss of complexity in human vocal anatomy as an adaptation for speech," Science **377**(6607), 760–763 (2022).

Pramanik, R., Verstappen, R. W. C. P., and Onck, P. R., "Computational fluid–structure interaction in biology and soft robots: A review," Phys. Fluids **36**(10), 101302 (2024).

Ringenberg, H., Rogers, D., Wei, N., Krane, M., and Wei, T., "Phase-averaged and cycle-to-cycle analysis of jet dynamics in a scaled up vocal-fold model," J. Fluid Mech. **918**, A44 (2021).

Scherer, R. C., De Witt, K. J., and Kucinschi, B. R., "The effect of exit radii on intraglottal pressure distributions in the convergent glottis," J. Acoust. Soc. Am. **110**(5), 2267–2269 (2001a).

Scherer, R. C., Shinwari, D., De Witt, K. J., Zhang, C., Kucinschi, B. R., and Afjeh, A. A., "Intraglottal pressure profiles for a symmetric and oblique glottis with a divergence angle of 10 degrees," J. Acoust. Soc. Am. **109**(4), 1616–1630 (2001b).

Scherer, R. C., Torkaman, S., Kucinschi, B. R., and Afjeh, A. A., "Intraglottal pressures in a three-dimensional model with a non-rectangular glottal shape," J. Acoust. Soc. Am. **128**(2), 828–838 (2010).

Sundström, E., Oren, L., Farbos de Luzan, C., Gutmark, E., and Khosla, S., "Fluid-structure interaction analysis of aerodynamic and elasticity forces during vocal fold vibration," J. Voice **39**, 293 (2025).

Tian, F.-B., Dai, H., Luo, H., Doyle, J. F., and Rousseau, B., "Fluid–structure interaction involving large deformations: 3D simulations and applications to biological systems," J. Comput. Phys. **258**, 451–469 (2014).

Titze, I., "Comments on the myoelastic—Aerodynamic theory of phonation," J. Speech Lang. Hear. Res. **23**, 495–510 (1980).

Titze, I. R. and Martin, D. W., "Principles of voice production," J. Acoust. Soc. Am. **104**(3), 1148 (1998).

Turek, S. and Hron, J., "Proposal for numerical benchmarking of Fluid-Structure interaction between an elastic object and laminar incompressible flow," in *Fluid-Structure Interaction*, edited by H.-J. Bungartz and M. Schäfer (Springer Berlin Heidelberg, 2006), Vol. 53, pp. 371–385.

Van Houtte, E., Van Lierde, K., D'Haeseleer, E., and Claeys, S., "The prevalence of laryngeal pathology in a treatment-seeking population with dysphonia," Laryngoscope **120**(2), 306–312 (2010).

Wex, C., Arndt, S., Stoll, A., Bruns, C., and Kupriyanova, Y., "Isotropic incompressible hyperelastic models for modelling the mechanical behaviour of biological tissues: A review," Biomed. Eng. **60**, 577 (2015).

Xue, Q., Mittal, R., Zheng, X., and Bielamowicz, S., "A computational study of the effect of vocal-fold asymmetry on phonation," J. Acoust. Soc. Am. **128**(2), 818–827 (2010).

Xue, Q., Zheng, X., Mittal, R., and Bielamowicz, S., "Computational study of effects of tension imbalance on phonation in a three-dimensional tubular larynx model," J. Voice **28**(4), 411–419 (2014).

Zhang, Z., Neubauer, J., and Berry, D. A., "Aerodynamically and acoustically driven modes of vibration in a physical model of the vocal folds," J. Acoust. Soc. Am. **120**(5), 2841–2849 (2006).

Zheng, X., Bielamowicz, S., Luo, H., and Mittal, R., "A computational study of the effect of false vocal folds on glottal flow and vocal fold vibration during phonation," Ann. Biomed. Eng. **37**(3), 625–642 (2009).

17 September 2025 16:03:22